MODELLING AND SIMULATION OF A PICO-HYDROPOWER OFF-GRID NETWORK

S. J. Williamson[+#], A. Griffo[*], B. H. Stark[+], J. D. Booker[+]

[+] Faculty of Engineering, University of Bristol, UK, BS8 1TR
[*] Dept. Electrical and Electronic Engineering, University of Sheffield, UK, S1 3JD
[#] Corresponding Author: sam.williamson@bristol.ac.uk

1.1. Introduction

Nearly 1 billion people who do not have access to electricity live in rural areas [1]. Extending the national power grid to many of these people is not feasible for technical or economic reasons. These typically remote communities therefore become reliant on local generation for their electricity supply. Diesel generators are the most popular alternative with low capital expenditure and well understood technology, but with significant and fluctuating maintenance and running costs. Therefore, renewable technologies - solar photovoltaics, wind, hydropower and biomass - are attractive for off-grid communities, as they can provide locally generated electricity from local resources.

Pico-hydropower is normally defined as electrical generation from a water resource with the capacity of less than 5 kW [2]. Where this resource exists, pico-hydropower is a suitable option for a community as it can operate over a range environmental conditions with different turbine designs, using simple and locally manufactured technology [3]. The output power is constant over short periods of time, varying over longer periods due to seasonal changes so there is no requirement for electricity storage. Pico-hydropower designs can be incorporated into already existing infrastructure, such as irrigation canals, with minimal environmental impact [4,5]. Once the initial capital cost of a pico-hydropower system is covered, the life-cycle cost is low, and produces low-cost power with high availability [6]. Typical pico-hydropower systems are operated in stand-alone configuration, with one unit feeding a number of houses. This system has no redundancy and is vulnerable to overload, such as the starting inrush current from an induction machine. There is also no opportunity of expansion as demand increases.

Creating a pico-hydropower network, as shown in Fig. 1, where identical units across a geographic area are electrically connected together, is desirable as it allows for a redundant, plug-and-play expandable system, with increased power generating capability allowing for both domestic and industrial loads. Each unit must rely on local measurements for control and be able to be maintained and serviced by local unskilled labour.

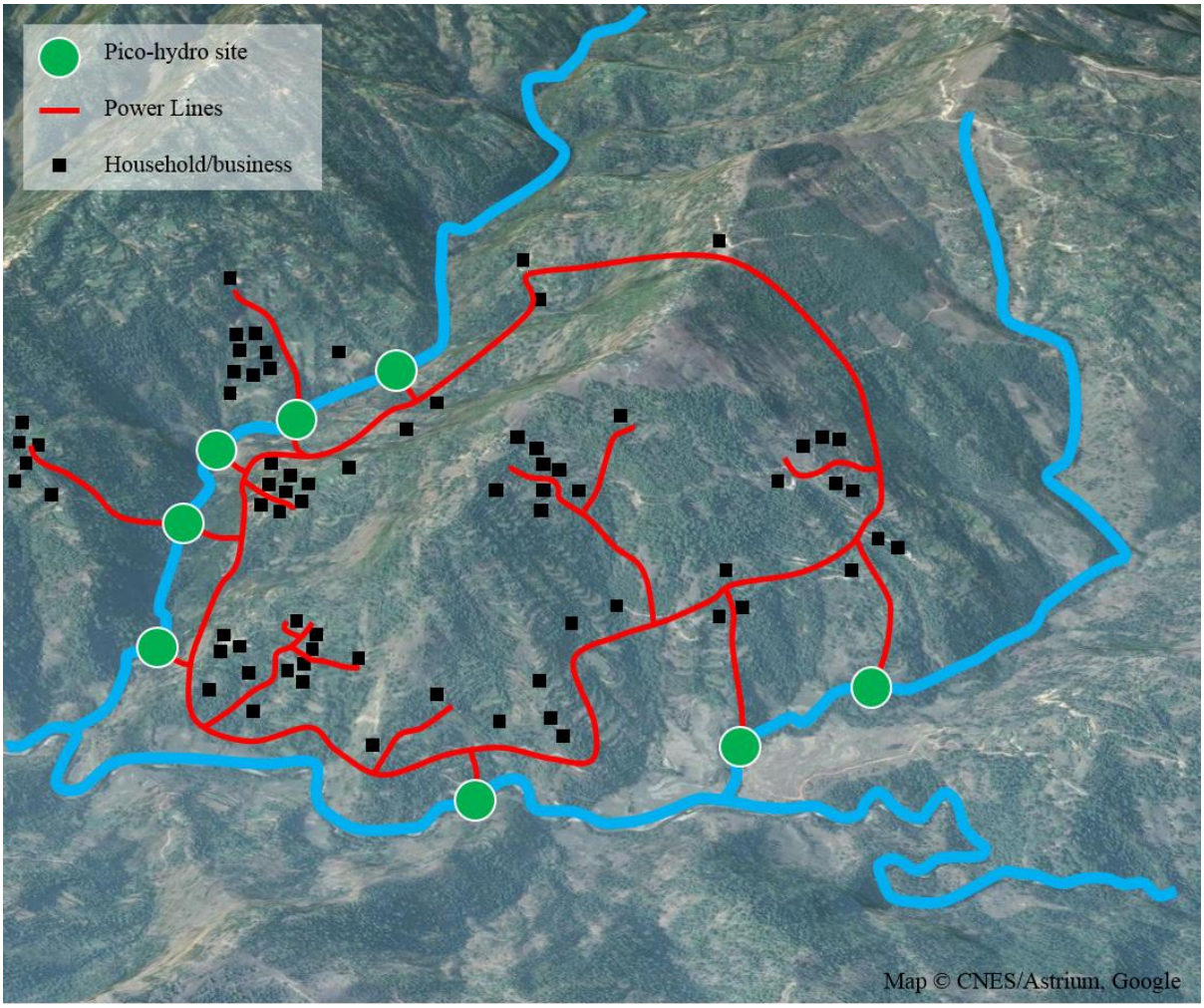

Figure 1: Off-grid pico-hydropower network concept.

This chapter will cover the system arrangement, modelling and control of such a system, with implementation of simulated example and expansion of the concept to include solar PV and wind turbine sources.

1.2. System Overview

The proposed pico-hydropower off-grid network is built up from a number of identical pico-hydropower generator units, with one or more installed at each turbine site dependent on the environmental conditions. As each site may have different environmental conditions, each unit may have different power available at the turbine, which may vary over time. The generator is interfaced onto the AC network through a power electronic AC-DC-AC interface, which allows a distributed grid, shown in Fig. 2. There is no communication between each unit, increasing the system reliability, so each unit must use local measurements to control the generator unit. This topology provides flexibility and redundancy in the network, making it suitable for a scalable and expandable system.

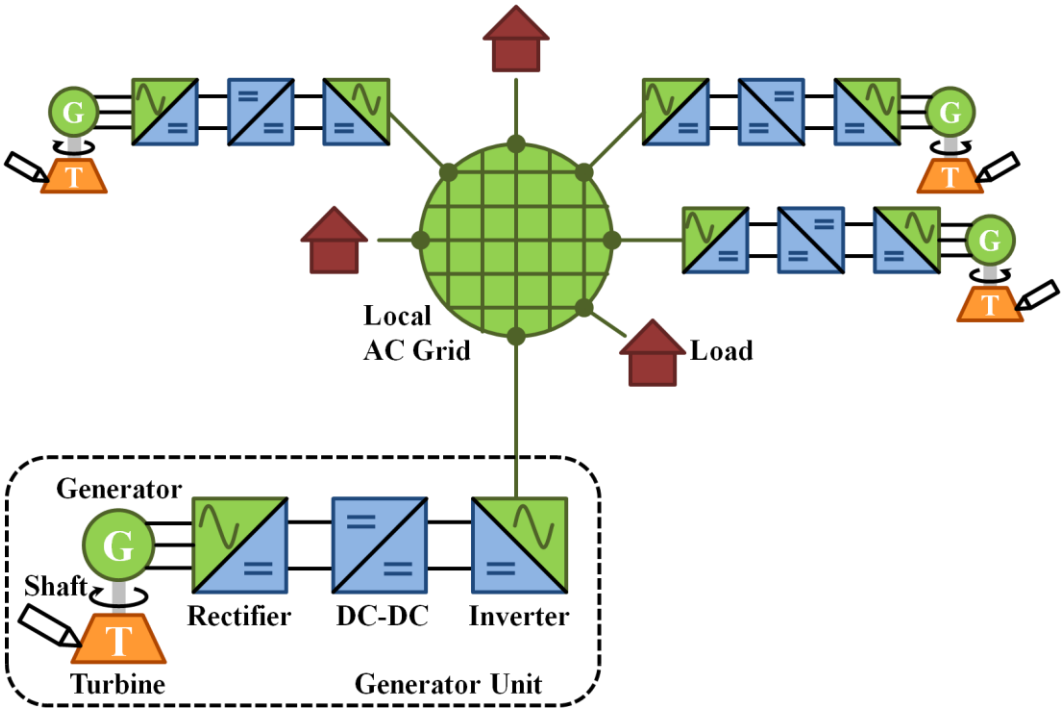

Figure 2: Distributed AC grid topology with non-communicating inverter front-ends.

This type of network is sometimes referred to as a multi-master system [7] as there is no central hub or single unit ensuring the network is properly controlled. Instead, each unit within the network has responsibility for voltage and frequency regulation, with the power sharing being a function of this control. This can lead to small swings in the grid voltage and frequency, with associated deviations in power sharing [8], but the major benefit is that there is no single point of failure, and the grid can naturally evolve over time without any input required to the existing installed units. The proposed network is made up of a number of generator units and loads, all connected by an AC local grid. The loads and generator units are interspersed geographically.

1.3. Component Models

The generator unit can be broken down into 6 different components; a turbine, an output drive shaft, a generator, a rectifier, a DC-DC converter, and a voltage source inverter, as shown in Fig. 2. Each of these components have an internal model which passes signals in the form of rotational speed, torque, voltage outputs or current draw between them, as shown in Fig. 3.

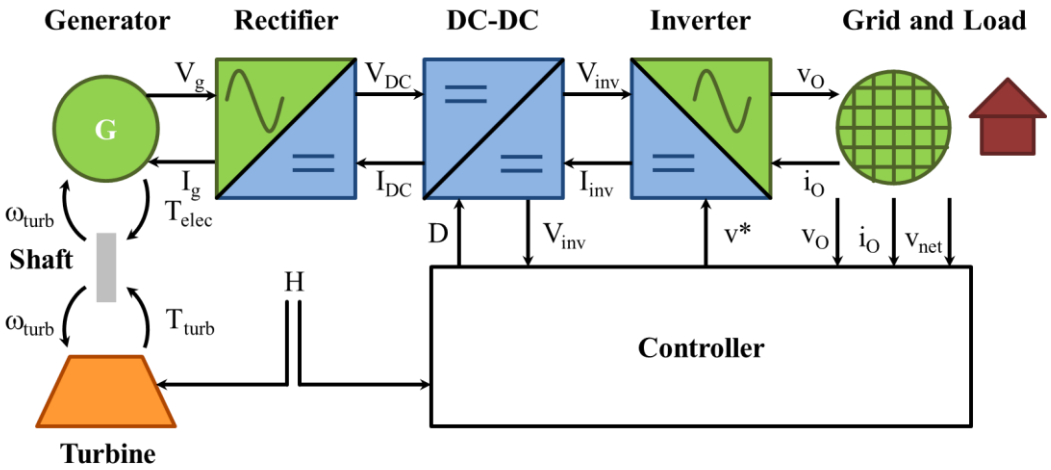

Figure 3: An overview of the complete model of a generator unit, with signal and control interactions between each component.

In modelling of the system, several assumptions are made. The water flow rate, and therefore head, at the site is usually assumed to be constant over a short time period (minutes) but will generally change over the longer term (hours), although an intake blockage would be an exception to this. The water flow passes through the penstock and nozzle to the turbine, which is directly connected to a 3–phase permanent magnet generator. The generator output is rectified to DC. As the turbine/generator will rotate at varying speeds dependent on load and head, a DC–DC converter with buck and boost capability is required to keep the DC link voltage at the inverter constant. A single–phase H–bridge inverter, with an LC filter to attenuate harmonics, connects the generator unit onto the AC grid (single phase, 50 Hz, 240 V_{RMS}).

The grid lines use standard Aluminium Conductor Steel Reinforced (ACSR) lines. The main load on a typical rural grid is lighting, with some power used for entertainment such as radios, televisions, computers and mobile phone charging. With a higher supply capacity, induction machines for agricultural processing and workshops are also used. Therefore, resistive-inductive and rectified, non-linear loads are used in the modelling.

1.3.1. Turbine

The turbine model has two requirements. Firstly, it must output the turbine torque for a given head and speed input, and secondly, from it, the maximum power available at the turbine must be able to be calculated. There are several models available in literature for hydro turbines [9-12], or alternatively if there is detailed experimental data, this could be used to determine the turbine performance.

For this work, a low-head Turgo turbine model, theoretically derived and experimentally validated in [9] is used. Using this, the maximum currently available turbine power can be calculated for the measured turbine head. The available torque and power characteristics as a function of the available head and turbine rotational speed used are shown in Fig. 4.

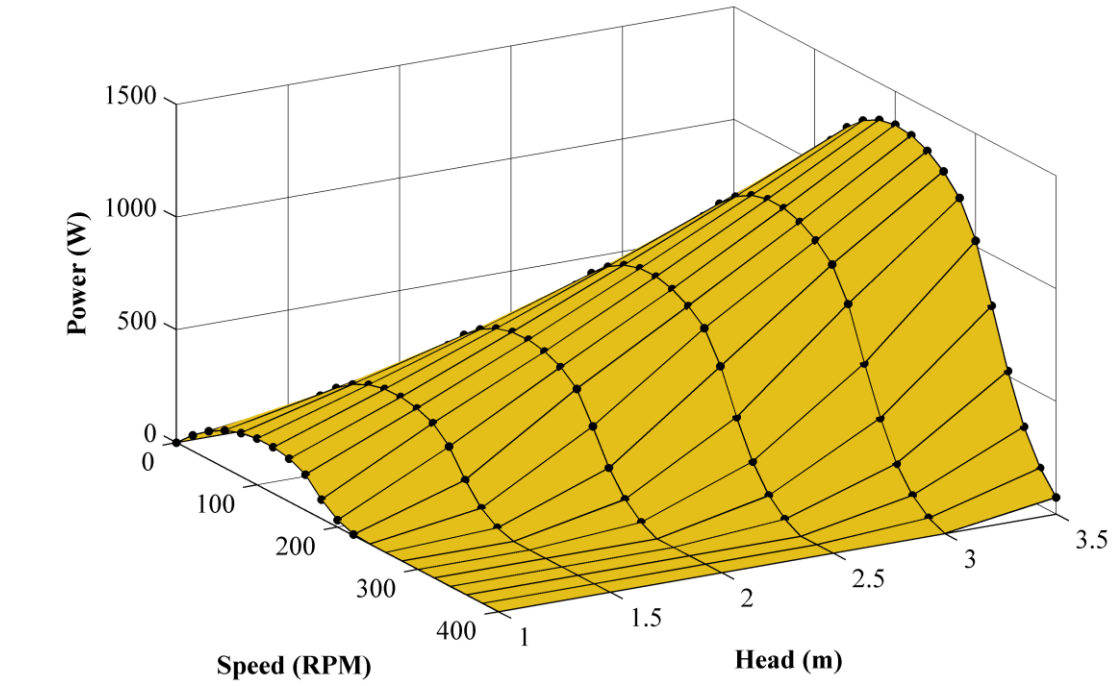

(a)

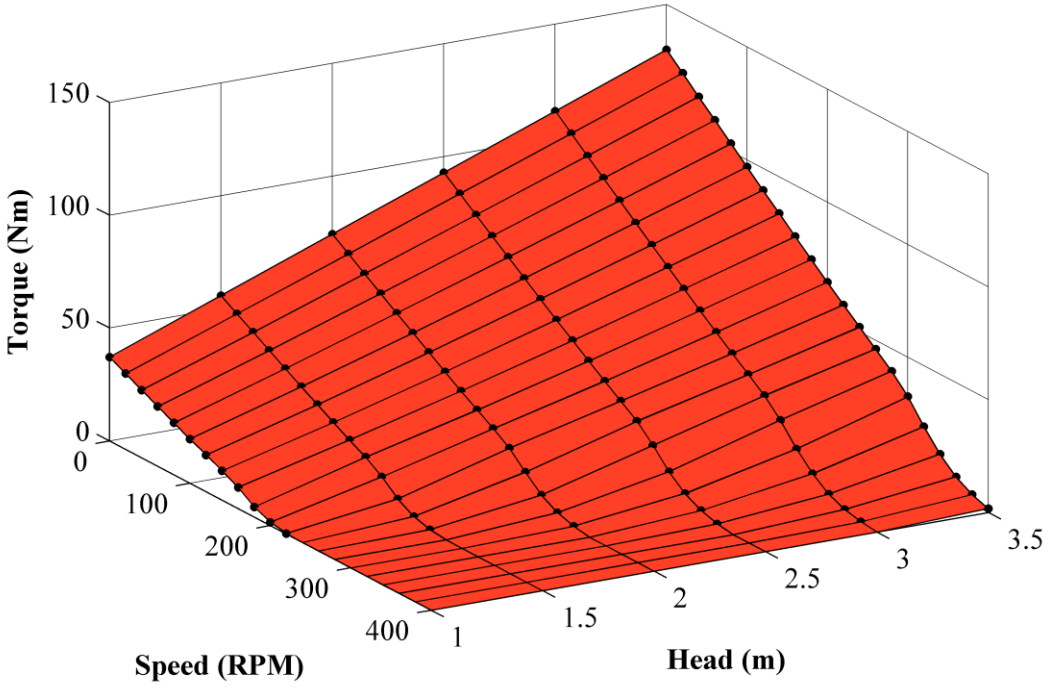

(b)

Figure 4: Theoretical (a) power and (b) torque models for a low-head Turgo turbine with the head ranging from 1.0 to 3.5 m [9].

The rotational speed is derived from the shaft model and the head is specified by the environmental conditions as an external input. The calculated turbine output torque is fed forward into the shaft model.

1.3.2. Shaft Assembly

The shaft assembly model describes the inertia of the turbine, generator rotor and the shaft itself. It receives the mechanical torque generated in the turbine and the electrical retarding torque from the generator, adds the damping torque from the drive train bearings and other resistances, to calculate the acceleration of the shaft according to

$$\frac{d\omega}{dt} = \left(\frac{1}{J}\right)\left(T_{turb} - T_{elec} - T_{damp}\right) \quad (1)$$

where J is the rotational moment of inertia of the complete drive train, T_{elec} is the electrical torque from the generator and T_{damp} is the damping torque which is proportional to the rotational speed. Using (1), the angular acceleration is integrated to obtain the rotational speed.

The shaft inertia is assumed to be negligible, with a relatively small radius of gyration compared to the turbine and generator, therefore the inertia is assumed to be the sum of the turbine and generator inertias. For the turbine, this inertia is estimated to be 0.47 kgm² [13].

1.3.3. Generator

The shaft model's rotational speed output ω_{turb} is fed into the generator model along with the current drawn I_g from the rectifier. The generator is modelled in the dq rotating reference frame using the following equations [14]

$$v_d = L_d\frac{di_d}{dt} + R_s i_d - L_q p\omega_{turb} i_q \quad (2)$$

$$v_q = L_q\frac{di_q}{dt} + R_s i_q - L_d p\omega_{turb} i_d + \lambda p\omega_{turb} \quad (3)$$

where v_d and v_q are the d- and q-axis voltages, L_d and L_q are the stator inductances referred to the d and q axes, R is the stator resistance, i_d and i_q are the d and q axis currents, p is the number of pole pairs, and λ is the permanent magnet flux. The voltages are converted from the dq reference frame to the 3-phase stationary coordinate system, and the output voltage amplitude, V_{gRMS}, is calculated and output to the rectifier. The electromagnetic torque from the generator is calculated by [14]

$$T_{elec} = 1.5p\lambda i_q \quad (4)$$

and is used in (1) to calculate the rotational speed of the shaft, ω_{turb}.

The machine to be modelled for this application is the PMGO-1,5K 1.5 kW permanent magnet generator by DVE Technologies [15]. Table 1 summarises the pertinent technical details of the machine. When rotating between 5-42 rad/s (50-400 RPM), the amplitude of the generator output voltage, $|V_g|$, ranges from 93 to 744 V.

Table 1: Generator technical data for simulation.

Parameter	Value
Output Rated Power	1.5 kW
Rated Output Speed	200 RPM
Number of pole pairs, *p*	9
Permanent Magnet Flux* λ	1.14 Vs
Resistance (phase) @ 20°C* R_s	4.75 Ω
Inductance (d and q axis)* L_d, L_q	0.11 H
Inertia J_{gen}	0.535 kgm²

*derived from datasheet

1.3.4. Rectifier

The 3-phase rectifier is modelled as a lossless rectifier converting the AC output from the generator to DC, and assuming unity power factor conversion. The rectifier output voltage is calculated by [16]

$$\mathrm{V_{DC}} = 1.35 \times V_{g,LL} = 2.34 \times V_{g,RMS} \quad (5)$$

The current draw from the generator can be calculated by equating the input and output power for the rectifier, such that

$$3 V_{g,RMS} I_{g,RMS} = V_{DC} I_{DC} \quad (6)$$

where V_{DC} and I_{DC} are the DC link voltage and current at the output of the rectifier. The DC link voltage is applied to the DC-DC converter and the peak current draw flows back to the generator.

1.3.5. DC-DC converter

The DC-DC converter is a buck–boost converter, as the rectifier will produce an output of between 265 V and in excess of 1 kV, as a function of the speed of the turbine and generator, and the inverter requires a constant DC link voltage of 400 V. A typical four-switch synchronous buck–boost converter topology is modelled, as shown in Fig. 5.

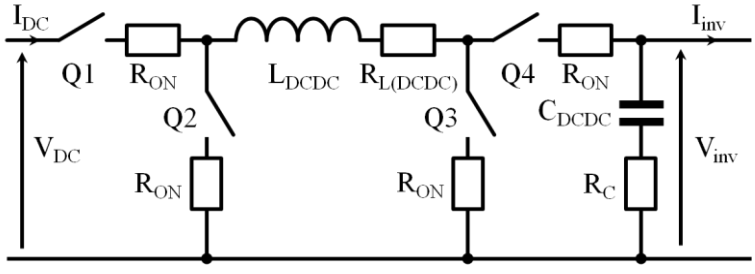

Figure 5: Four-switch buck-boost converter.

The converter is assumed to operate in continuous current mode. The modelling equations for the converter have been derived using the state–space averaging method [17].

$$L_{DCDC}\frac{di_L}{dt} = D\left(-\left(2R_{ON} + R_{L(DCDC)}\right)i_L + V_{DC}\right) + (1-D)\left(-\left(2R_{ON} + R_{L(DCDC)}\right)i_L - v_C + R_C I_{inv}\right) \quad (7)$$

$$C_{DCDC}\frac{dv_C}{dt} = D(-I_{inv}) + (1-D)(i_L - I_{inv}) \quad (8)$$

$$V_{inv} = \mathrm{D}(v_C - R_C I_{inv}) + (1-\mathrm{D})(R_C i_L + v_C - R_C I_{inv}) \quad (9)$$

$$I_{DC} = \mathrm{D}(i_L) \quad (10)$$

where L_{DCDC} is the inductance, i_L is the current through the inductor, D is the duty ratio, R_{ON} is the resistance of the switches in the on state, $R_{L(DCDC)}$ is the resistance of the inductor, R_C is the series resistance of the capacitor, C_{DCDC} is the output capacitor, v_C is the voltage across the capacitor, and V_{inv} and I_{inv} are the output voltage and current of the converter. The values for the components used in the simulation are shown in Table 2.

Table 2: DC-DC converter technical data for simulation.

Parameter	Value
Inductance, L_{DCDC}	10 mH
Inductor Parasitic Resistance $R_{L(DCDC)}$	0.05 Ω
Capacitance, C_{DCDC}	100 μF
Capacitor Equivalent Series Resistance $R_{C(DCDC)}$	0.1 Ω
Switch On-state Resistance R_{ON}	0.05 Ω

It is assumed that there is no reverse recovery current or dead time requirement in the switching. From this model, the output voltage of the DC-DC converter is passed to the inverter, and the current I_{DC} is passed back to the rectifier.

1.3.6. Inverter Modelling

The inverter is modelled using an ideal controlled voltage source in SimPowerSystems. This assumes that the inverter has an infinite control bandwidth, so it is able to follow the reference signal exactly, and any high frequency switching noise is eliminated by the output filter. The inverter is assumed to have a maximum output power of 1.5 kW, thus providing margin to allow for short power spikes. The efficiency of the inverter is modelled using the equations and parameters derived in [18], assuming a type 2 inverter which has a good efficiency characteristic over a range of loads,

$$\eta_{inv} = \frac{p}{p + p_0 + kp^2} \quad (11)$$

where

$$p = \frac{P_{inv,out}}{P_{inv,rated}}$$
$$p_0 = 0.0072$$
$$k = 0.0345$$

The voltage from the inverter, V_{RMS}, is fed into the grid, whilst output current demand, I_{RMS}, is measured and divided by the inverter efficiency before being applied to the DC-DC converter as the demand current I_{inv}.

1.3.7. Transmission Line and Load Modelling

The ACSR grid lines are modelled as impedances. The chosen lines have a cross-sectional area of 21 mm², with a resistance of 1.41 Ω/km and reactance of 0.32 Ω/km when conductors are 0.3 m apart [19]. The linear load is modelled as an impedance with a lagging power factor of 0.9, representing a loaded induction machine running with some resistive load [20]. The non-linear load is modelled with a diode bridge rectifier and capacitor with a load resistor.

1.4. Control Scheme Design

1.4.1. Turbine and DC-DC Converter Controller Design

From (1), it can be seen that excess turbine torque accelerates the drive train, and conversely as more load is drawn from the generator unit, the drive train slows down. The power curve for the turbine is similar to those shown in Fig. 4 (a). Beyond a certain loading, where the turbine has slowed to its maximum power speed, ω_{CRIT}, further load reduces the turbine power and the system becomes unstable and stalls. A control system is required to restrict the turbine rotational speed exceeding ω_{CRIT}. This can be implemented by measuring output power and speed from the generator and reacting if both the power and rotational speed are decreasing simultaneously by limiting the current output through the rectifier. The output voltage of the DC–DC converter, V_{INV}, is regulated to 400V by using a PI compensator.

1.4.2. Inverter Control Design

The inverter control system is critical to ensure the operation of the off-grid network. It must be able to regulate the voltage and frequency using only local measurements, provide the plug-and-play capability for the system, allow good power sharing between units based on the power available at the turbine, and ensure a good power quality of the output voltage. The following paragraphs describe the design of this controller in detail, with an overview of the control system shown in Fig. 6.

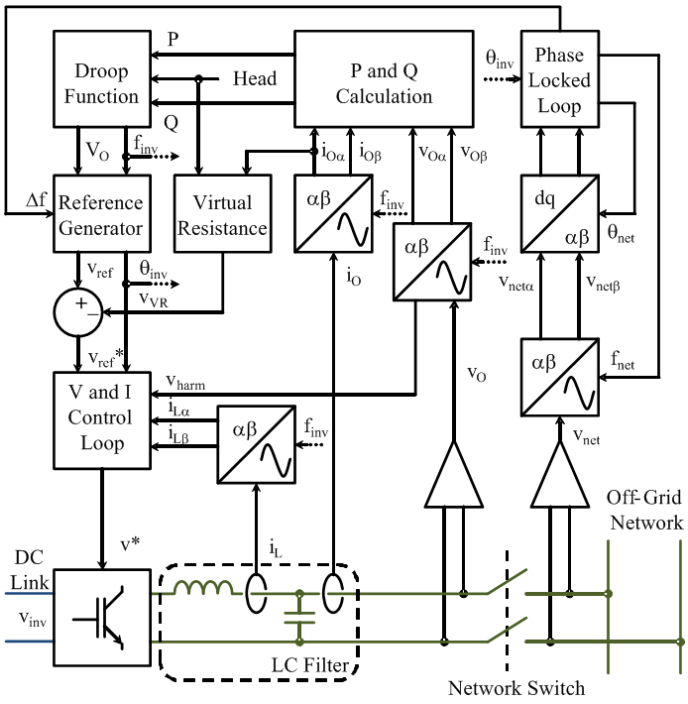

Figure 6: Control System Structure

1.4.2.1. Voltage and Frequency Regulation via Droop Control

Droop control adjusts the output voltage and frequency of an inverter in order to establish a desired relationship between supplied active and reactive power and measured local voltage and frequency. The relationships depend on the line and inverter output impedances [21]. Typically, transmission lines are considered to be inductive, e.g. in [7], however the network considered here operates at low voltage (240 V_{RMS}) therefore resistive lines are assumed and the droop equations are [8]

$$f = f_0 + mQ \tag{12}$$

$$V_O = V_{O,0} - nP \tag{13}$$

where f is the output frequency, f_0 is the output frequency set point, m is the reactive power droop coefficient, Q is the measured reactive output power, V_O is the output voltage reference, $V_{O,0}$ is the output voltage set point, n is the active power droop coefficient and P is the measured active power. Although this relationship is designed for a low-voltage, resistive-line network to be used with identical controllers, it has been shown to also operate in conjunction with inductive- or capacitive-line based droop control [22].

The droop coefficient is in the forward path of the controller, therefore the transient response of the control is dependent on droop coefficients, m and n [8]. Ideally, these should be large to have good transient response and also allows for accurate power sharing, but this would cause a large variation in the regulated voltage and frequency. The regulation is also typically defined in the system specification, fixing the droop coefficients. Therefore, to improve the transient response of the control system, additional terms can be included. In this system a differential term is included in the droop equations, as described in [8], as integral terms can cause instabilities with resistive line droop equations. Therefore (12) and (13) become

$$f = f_0 + mQ + m_d \frac{dQ}{dt} \tag{14}$$

$$V_O = V_{O,0} - nP - n_d \frac{dP}{dt} \tag{15}$$

where m_d and n_d are the differential constants. The reference voltage waveform is then constructed from these values of output voltage and frequency.

The impedance of the transmission lines in off-grid networks and the inverter output impedance are neither purely inductive nor resistive which leads to cross-coupling in the droop function [21]. A virtual output impedance can be used to force these to appear either inductive or resistive, dependent on the control scheme selected, and allow the droop function to be completely decoupled [8]. In this scheme, as resistive lines are assumed, this is achieved by multiplying the fundamental component of the measured output current i_O by a virtual resistance gain R_V and then subtracting this from the reference voltage calculated by the droop function.

1.4.2.2. Power Sharing

Standard droop control, utilizing steep droop coefficients, is able to share power well with units that have equal rated power. However, when there are unequally rated units on the system, then the power sharing is not proportional to the rated output of the system, so smaller units will have a larger proportion of their output supplied to the system. The droop coefficients and virtual resistance can be made dependent upon the input power, which assists in achieving accurate power sharing proportional to the unit's available input power [23,24], which have been used for UPS inverters. In the presented case, the input power is dependent on the head at the turbine.

From this, a normalized turbine power output, the ratio of $P_{TURB,MAX}(H)$ to the maximum possible turbine output power $P_{TURB,MAX}$, a fixed value, can be written as

$$\gamma = P_{TURB,MAX}(H)/P_{TURB,MAX} \quad (16)$$

Then the droop coefficients and virtual resistance are set to

$$m = m_{MAX}/\gamma \quad (17)$$
$$n = n_{MAX}/\gamma \quad (18)$$
$$R_V = R_{V,MAX}/\gamma \quad (19)$$

where m_{MAX} and n_{MAX} are defined from the regulated range of frequency and output voltage and the maximum output active and reactive powers and $R_{V,MAX}$ is the maximum power virtual resistance. In this way, as γ reduces the gradients of the droop curves become steeper. So in the case of the P vs. V_O droop curve, for the same output voltage, the active power delivered is reduced.

1.4.2.3. Power Measurement

The droop function, (14) and (15), needs the line-cycle-averaged active and reactive powers to calculate the output voltage and frequency. In 3-phase systems this can be achieved by using the Clarke's transform [25] to convert the line values into orthogonal α and β components. The instantaneous powers are calculated using

$$P = \left(v_{O\alpha} i_{O\alpha} + v_{O\beta} i_{O\beta}\right)/2 \quad (20)$$
$$Q = \left(v_{O\beta} i_{O\alpha} - v_{O\alpha} i_{O\beta}\right)/2 \quad (21)$$

which are used as inputs for the droop function. For single-phase systems, there are several different methods to achieve the conversion between a single-phase sinusoidal signal and $\alpha\beta$ components, such as shifting the signal by 90° using a transport delay [8], integrating the incoming signal [26] or using a resonant filter [27], which is based on a Second Order Generalised Integrator (SOGI) [28]. A modified version of this SOGI-based filter is proposed in [29], where an additional gain is included in the orthogonal (β) path, and the gains are calculated using a Kalman function. The method used in this approach has an identical structure to that presented in [29], but with constant gain values. The resonant frequency used in the filter is calculated from the droop function, (3), and is fed into the filter, allowing the filter to adapt to any variation in the grid frequency. The structure of the SOGI-based filter is shown in Fig. 7 (a).

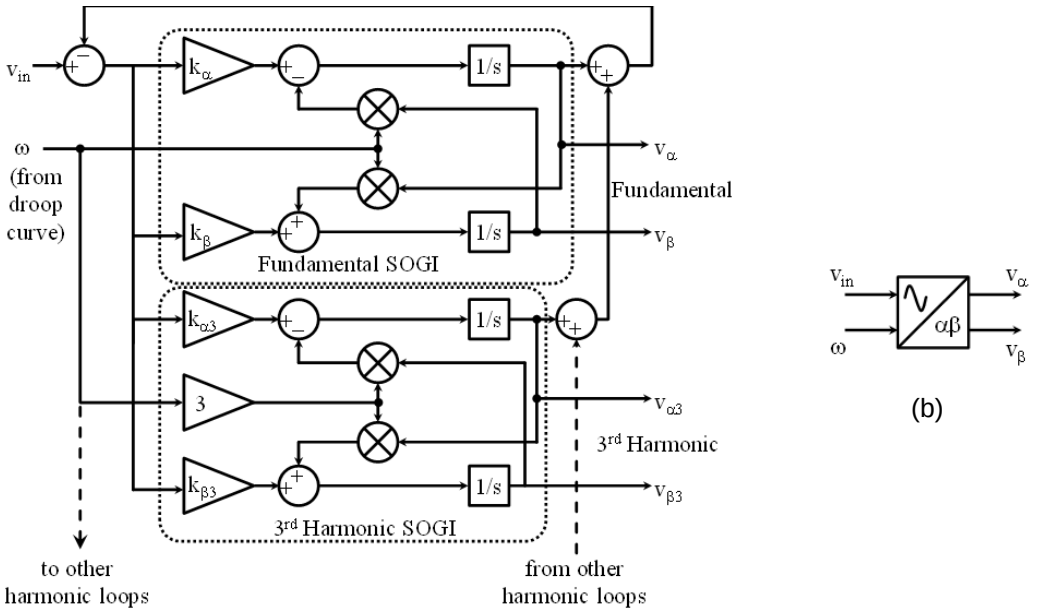

(a)

Figure 7: (a) Second Order Generalised Integrator (SOGI) based filter with additional harmonic loops. (b) Symbolic representation of SOGI-based filter.

Additional resonant loops can be added to filter any harmonics in the input [29], as shown in Fig. 7 (a) where a 3rd harmonic loop is included. The harmonics from each additional loop can be extracted and used if needed. Fig. 7 (b) shows the symbol used for the SOGI-based filter in the following Sections.

1.4.2.4. Fundamental Voltage Controller

A second order LC filter is assumed at the output of the inverter. Similar to the control structure commonly employed in three-phase grid connected inverters and active rectifiers [30,31], a synchronous reference frame controller is employed here for both the outer output capacitor voltage and inner inductor current control loops. A similar approach has been used in [32] where the outer voltage loop is transformed into the synchronous frame, before being returned into the stationary frame for the current control loop. This current loop is a proportional loop with a feed-forward term, which reduces the need for a large gain to reduce the steady-state error. Similar control strategies are proposed in [33-35], where the systems described are either already in three-phase or use delays to create the orthogonal component.

Here, the control scheme shown in Fig. 8 is employed to control the inverter output voltage. This is different to [32] as it uses the synchronous reference frame throughout the control of voltage and current, allowing simple PI control to be used in both and ensuring a zero steady state error. Reference [33] uses the synchronous reference frame throughout the controller, but the presented controller differs as the reference voltage generated from the droop function and measured voltage and currents are transformed into the dq synchronous reference frame using the SOGI-based filter. The $\alpha\beta$ to dq transform, and inverse, is synchronized with the angle fed forward from the droop equations, (14), not through a PLL loop as normally used. PI loops are then used to force the measured d-axis voltage to its reference and the q-axis voltage to zero.

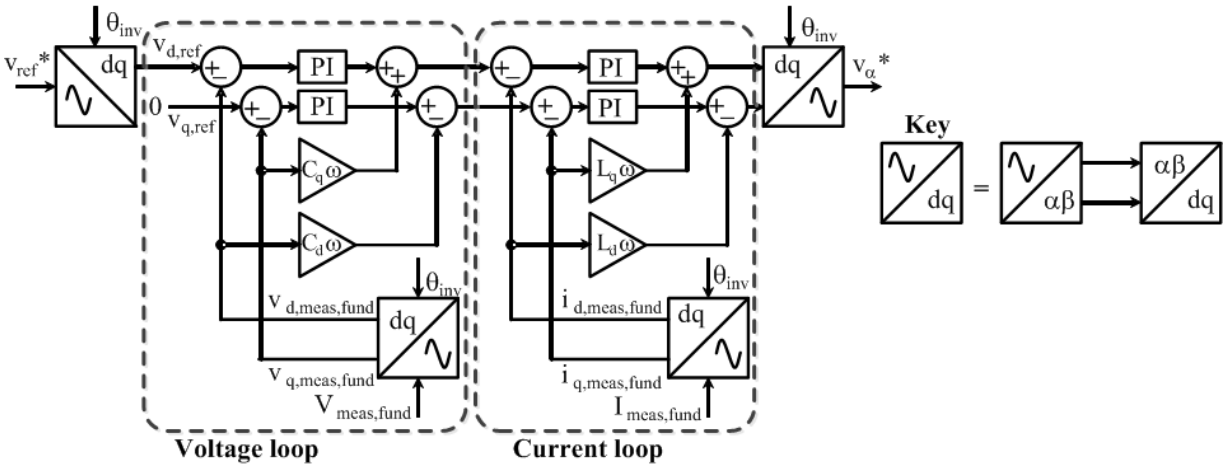

Figure 8: Proposed voltage and current controller using synchronous reference frame.

1.4.2.5. Harmonic Voltage Controller

In single-phase applications, harmonic distortion compensation has been proposed in [36] where band-pass virtual resistances are employed at the point of common coupling, providing a power filter prior to the load. In three-phase grid connected inverters and active power filters applications, harmonic compensation using a series of synchronous frame harmonic voltage PI controllers, or Proportional-Resonant controllers have been proposed in [30,31,37,38]. Similar to the three-phase strategies, here the output voltage harmonics are suppressed using a series of synchronous frame harmonic voltage PI controllers at the inverter output, as with the fundamental voltage controller described above. As shown in Fig. 9, the measured harmonic output voltages, extracted from the SOGI-based filters in Fig. 7, are transformed into the dq reference frame. Using a PI controller, the measured harmonic voltages are forced to zero. These are transformed back into the $\alpha\beta$ reference frame, and the α component becomes the reference waveform from the harmonic. All the harmonic reference waveforms are summed to form the final reference, which is output to the PWM generator.

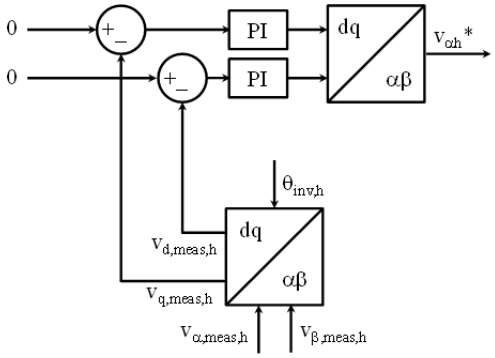

Figure. 9: Harmonic voltage controller in synchronous reference frame

1.4.2.6. Phase Locked Loop (PLL)

The standard way of synchronization is for the network voltage to be transformed into the synchronous reference frame via the $\alpha\beta$ stationary reference frame, with the network angle found by forcing the q-axis component to zero. Advanced PLL strategies are presented in [28,39-43], using a synchronous reference frame or digital non-linear methods. Here, a synchronous reference frame based PLL is used, with a single-phase input. The transformation of the voltage signal from a single-phase signal to the $\alpha\beta$ reference frame can be achieved using the SOGI-based filter again, as in [28] and analysed in [39], and shown in Fig. 10.

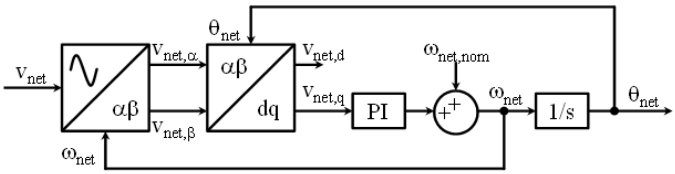

Figure 10: SOGI-based phase-locked loop.

The off-grid network angle θ_{net} is then compared with the inverter angle θ_{inv}. This error is fed to a proportional controller and then back into the droop function to change the frequency of the inverter to match the grid frequency. Once the error is below the critical value ε_{crit}, the switch between the inverter and the grid is closed with a latch to ensure that there is no chattering.

1.5. Simulation Results

The simulations of a basic pico-hydropower off-grid network are carried out for a pair of generator units connected to an AC bus bar, with linear and non-linear loads on the bus, as shown in Fig 11, using the models and control described in the previous sections. These simulations will identify how the different systems react to changes in load and environmental (head and flow) conditions.

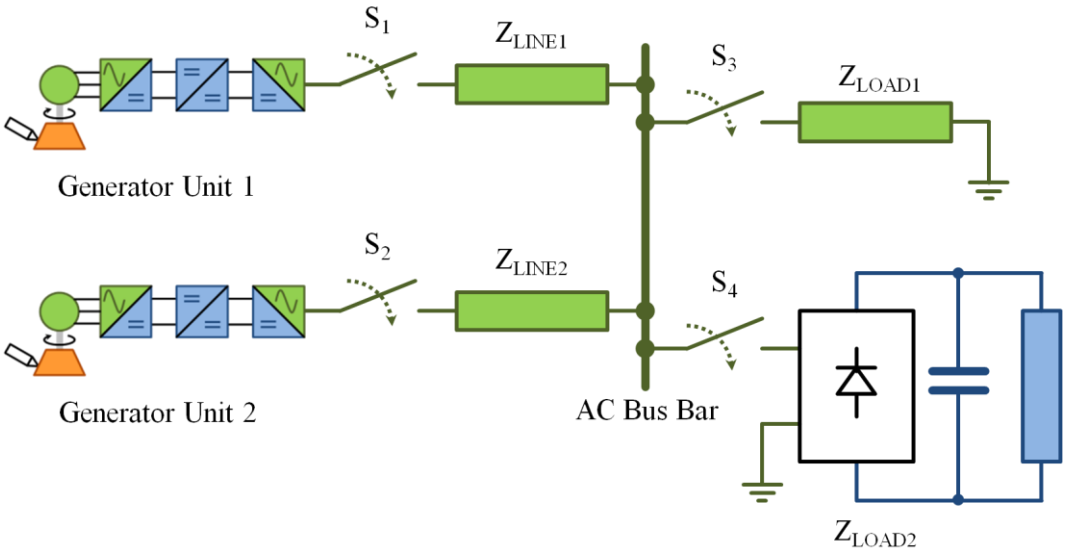

Figure 11: Layout of two generator units used in simulations, with each unit connected to the AC bus bar via an impedance, and a linear and non-linear load connected to the bus.

1.5.1. Single Generator Unit with Varying Load

The first simulation is to show the response of the system to a changing load. Using the layout in Fig. 11, only generator unit 1 is used, with a load that changes from 500 VA to 750 VA and then back down to 250 VA, all at a power factor of 0.9. Initially, S_1 and S_2 are closed. The results from this simulation are shown in Fig 12.

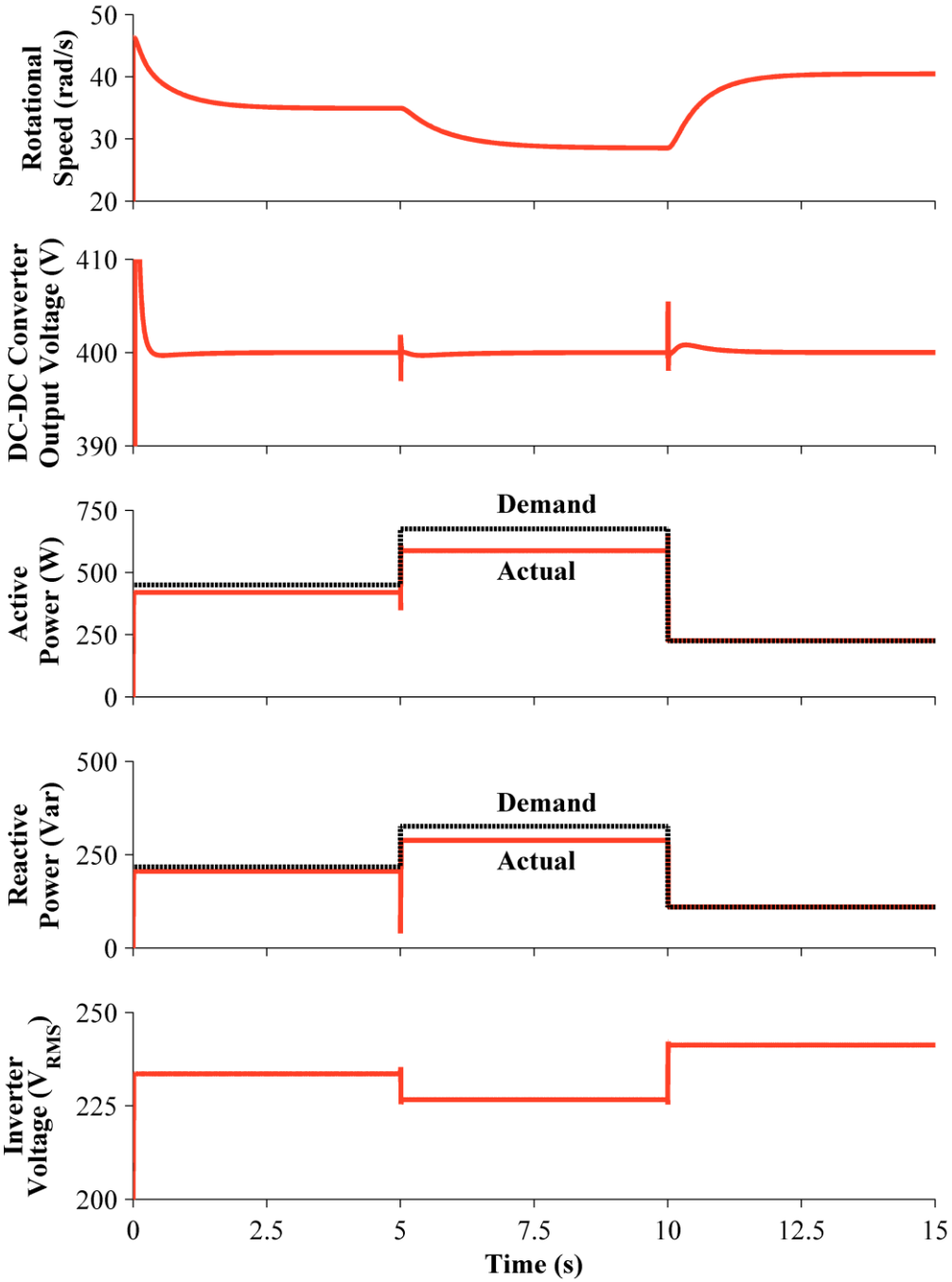

Figure 12: Response of a single generator unit to a varying load (500 VA, 750 VA, 250 VA) with turbine/generator rotational speed, DC-DC converter output voltage, active power, reactive power and inverter output voltage RMS.

At t = 0 there is no load on the inverter, therefore the turbine is at free-wheeling speed. When the load is added at t = 0 the rotating components slow, but the inertia of the turbine and generator cause the deceleration to last 2 seconds. This constant slowing over 2 seconds means that the input voltage to the rectifier, and therefore the DC-DC converter, is not constant and is slowly reducing, although it can be seen that DC-DC converter is able to maintain a constant output voltage once it has achieved its reference value, even during this input voltage change. As the power demand increases at t = 5 s, the voltage and frequency droop, and the speed of the rotating components drop further to match the turbine output power with the demand from the inverter. Although there is a small oscillation in the DC-DC converter output voltage and inverter output voltage, these return to a steady state quickly.

At t = 10 s, the power demand reduces again, so the rotational speed increases, as does the output voltage from the inverter, while the DC-DC converter output voltage remains constant after a small oscillation.

The output power is slightly lower than the demand during the periods of high demand due to the droop from the control system, and the further reduction in inverter output voltage due to the virtual resistance, with the power demand calculated on the nominal power output from the inverter.

1.5.2. Performance with Non-Linear Load

Generator unit 1 is then connected to a non-linear load, a diode rectifier with a 3300 μF smoothing capacitor and a 100 Ω resistor, with S1 and S4 closed. The voltage waveforms obtained for this simulation are shown in Fig. 13.

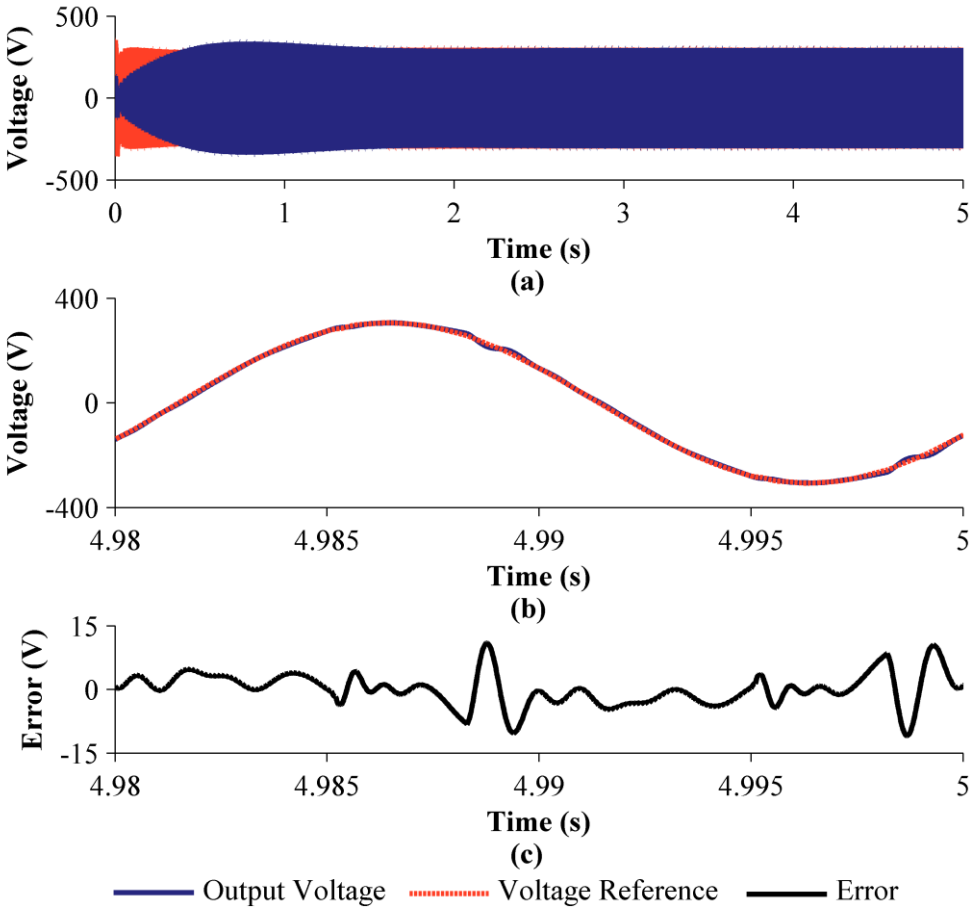

Figure 13: (a) Inverter output voltage tracking with a non-linear load (diode rectifier with 3300 μF capacitor and 100 Ω resistor), complete voltage profile over 5 s from inverter switch on. (b) Voltage reference vs. inverter output voltage (c) The error between the reference and output voltage.

There are some harmonics in the output voltage waveform, due to the current harmonics drawn from the load. The error has a high frequency and irregular oscillatory nature. The peak amplitude of this error is approximately ±11 V which is approximately 3.6% of the peak voltage.

1.5.3. Power Sharing Performance

The following two simulations are for two generator units connected in parallel. The first simulation has two generator units with equal line impedance between the generator unit and the AC bus bar, with switches S_1-S_3 in Fig. 11 closed. The load starts at 500 VA, increasing to 1500 VA at t = 5 s, and then reduces to 1000 VA at t = 10 s, all with a power factor of 0.9. The results for this can be seen in Fig. 14.

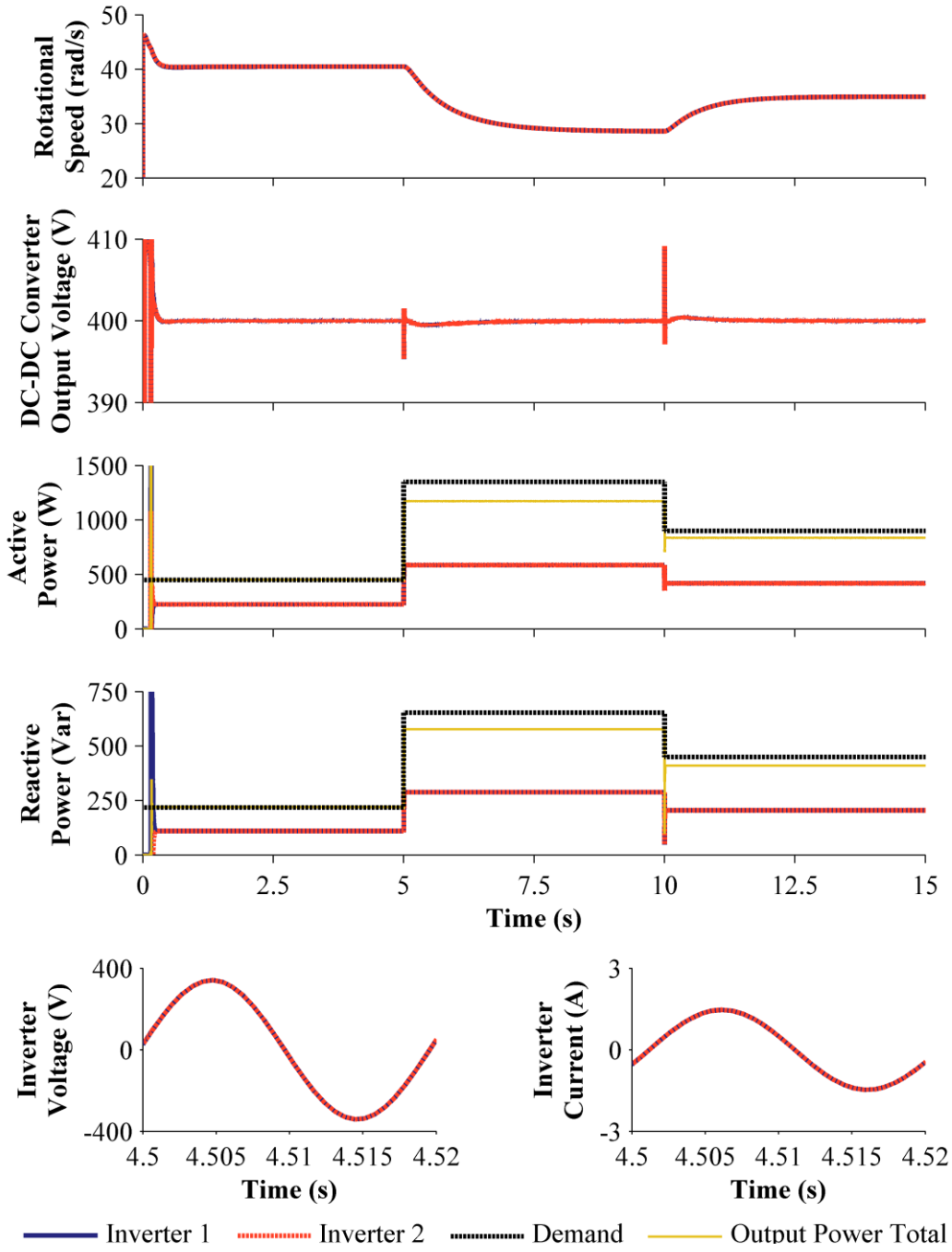

Figure 14: Simulation of two generator units with equal line impedance to an AC bus bar feeding a load varying from 500 VA at t = 0 s to 1500 VA at t = 10 s, then reducing to 1000 VA at t = 10 s.

As can be seen, the two systems share the load equally, delivering an equal current to the load and the turbine rotational speed identical. When the line impedances are not equal, with Z_{LINE2} twice size of Z_{LINE1}, the results of the simulation are shown in Fig. 15.

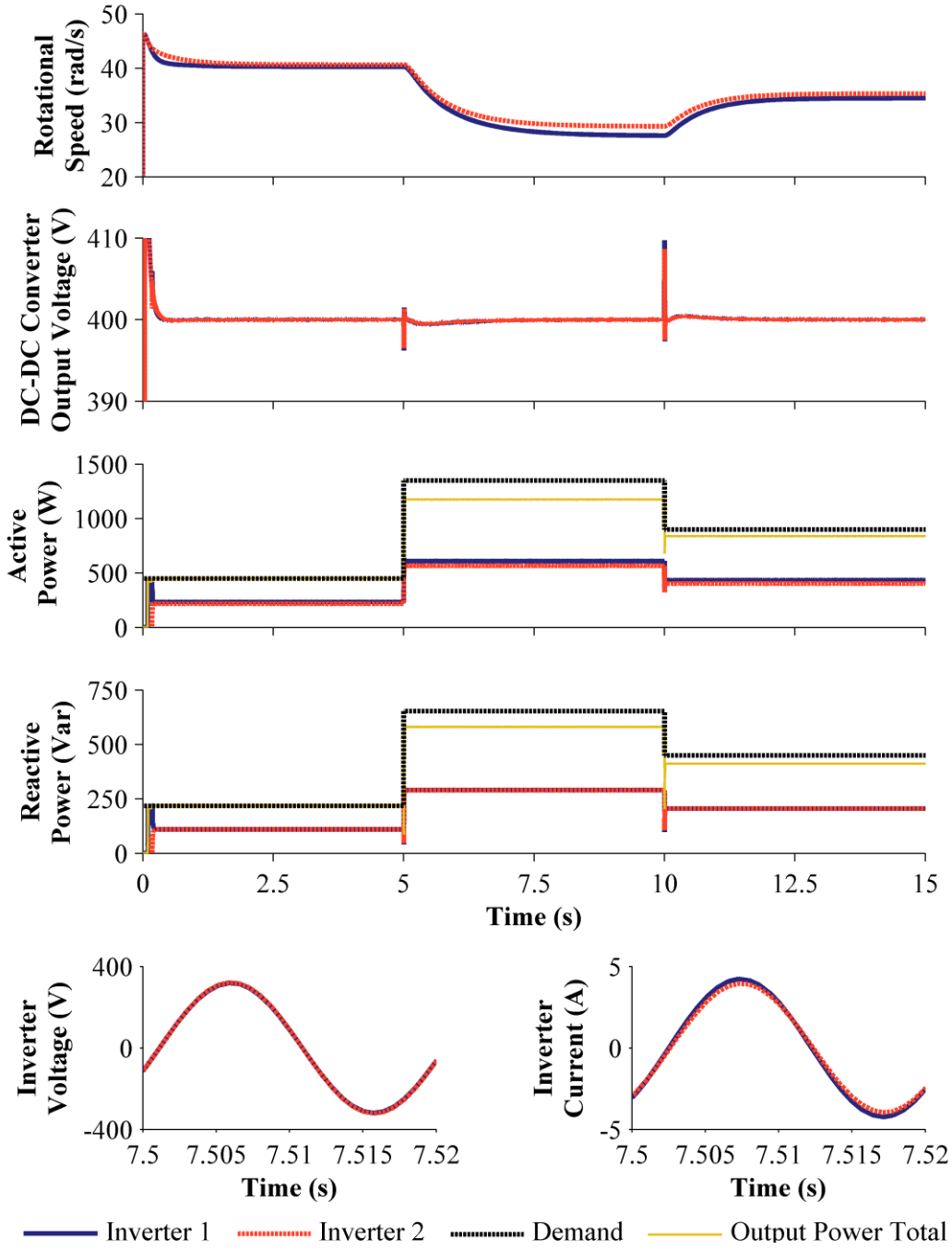

Figure 15: Simulation of two generator units with unequal line impedance ($Z_{LINE2} = 2 \times Z_{LINE1}$) to an AC bus bar feeding a load varying from 500 VA at t = 0 s to 1500 VA at t = 10 s, then reducing to 1000 VA at t = 10 s.

In this simulation, as generator unit 1 is closer to the load, it takes a slightly higher proportion of the active power demand, therefore the rotational speed of the turbine and generator is slower. As the reactive power is dependent on the frequency, both generator units share this equally. Increasing the load after 5 s causes the power sharing difference between the two units to rise, increasing the imbalance in supplied load current from each unit.

1.5.4. Change in Input Power (Drop in Head)

In this simulation, the head at generator unit 1 remains constant at 3 m, but the head at generator unit 2 starts at 3.5 m, before reducing linearly to 2 m over a 5 second period. The line impedances to the AC bus bar are not equal, generator unit 1 has a line impedance half that of generator unit 2. The load remains constant at 500 VA. The results for this simulation are shown in Fig. 16.

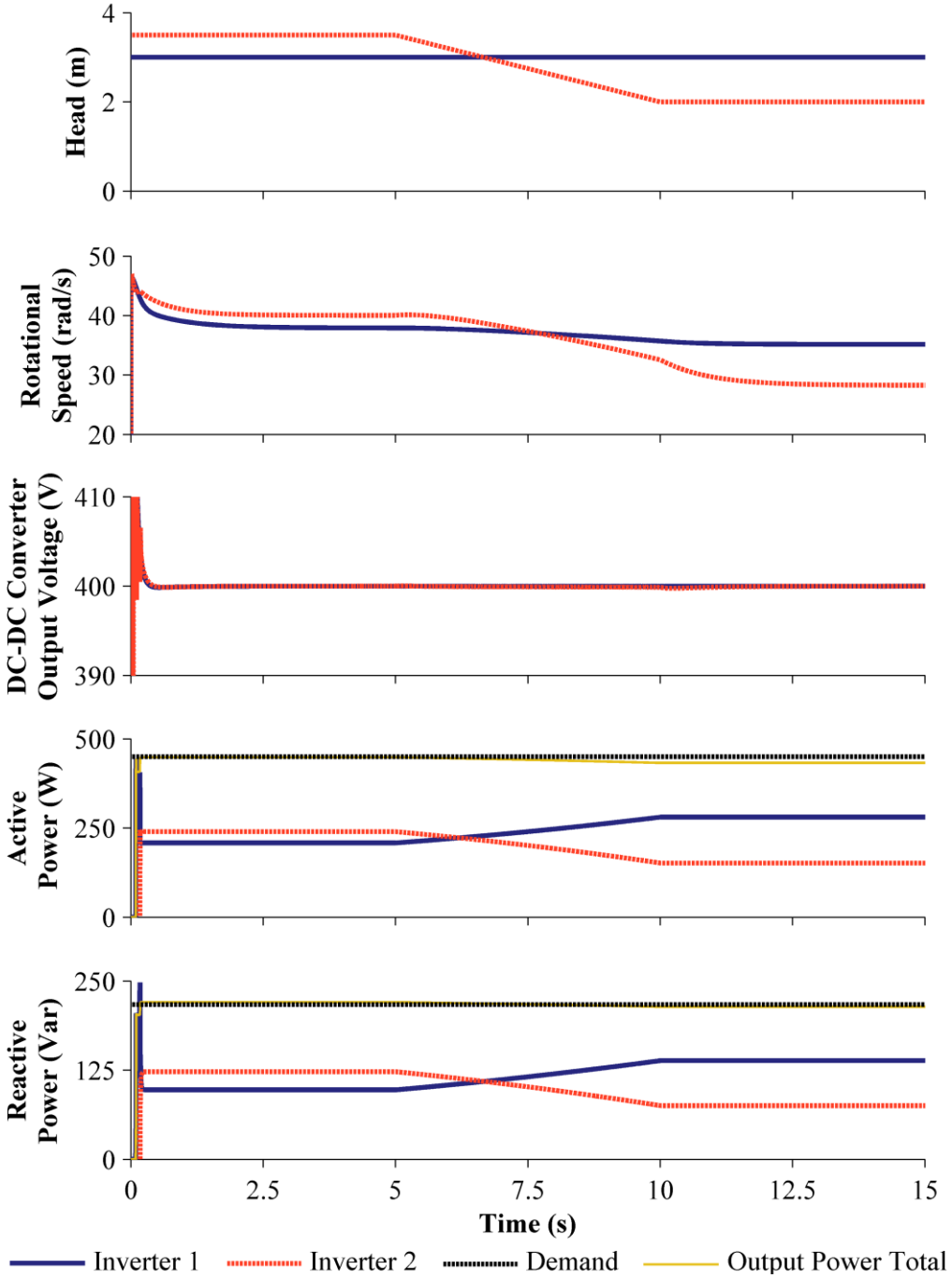

Figure 16: Simulation of two generator units with a head change from 3.5 to 2 m on generator unit 2 with a varying load and unequal line lengths.

As the head reduces at generator unit 2, generator unit 1 provides more of the power demand. The DC-DC converter is able to compensate for the drop in generator voltage, and

its control keeps the output at the regulated value. These results show that the system remains stable and is able to cope with a change in head at one unit.

1.6. Modelling of Implementation in Nepal

The system is envisioned to operate in many locations all over the world where there is no electricity supply from the national power grid and suitable water resources, in both developed and developing countries. An example implementation of the off-grid pico hydro network is shown in the following simulation.

The example implementation environment is located in Bhanbhane district, Gulmi, Western Nepal. A map of the area is shown in Fig. 17 with the layout. The Patan River has 5 potential pico hydro sites along it, which are detailed in Table 3.

Table 3: Details of the possible site locations in Bhanbhane District, Western Nepal (minimum flow and head data).

Site No.	Name	Min. Flow (l/s)	Head (m)	Latitude	Longitude	Min. Power Output (kVA)
1	Badachaur Pokherel	35	3.3	28°6'47"	83°6'15"	0.69
2	Hadhade	35	3.5	28°6'42"	83°6'30"	0.74
3	Badachaur	35	5.0	28°6'39"	83°6'37"	1.05
4	Bharji	35	2.5	28°6'44"	83°6'49"	0.53
5	Badachaur School	35	2.5	28°6'55"	83°7'9"	0.53
				Total Power		**3.54**

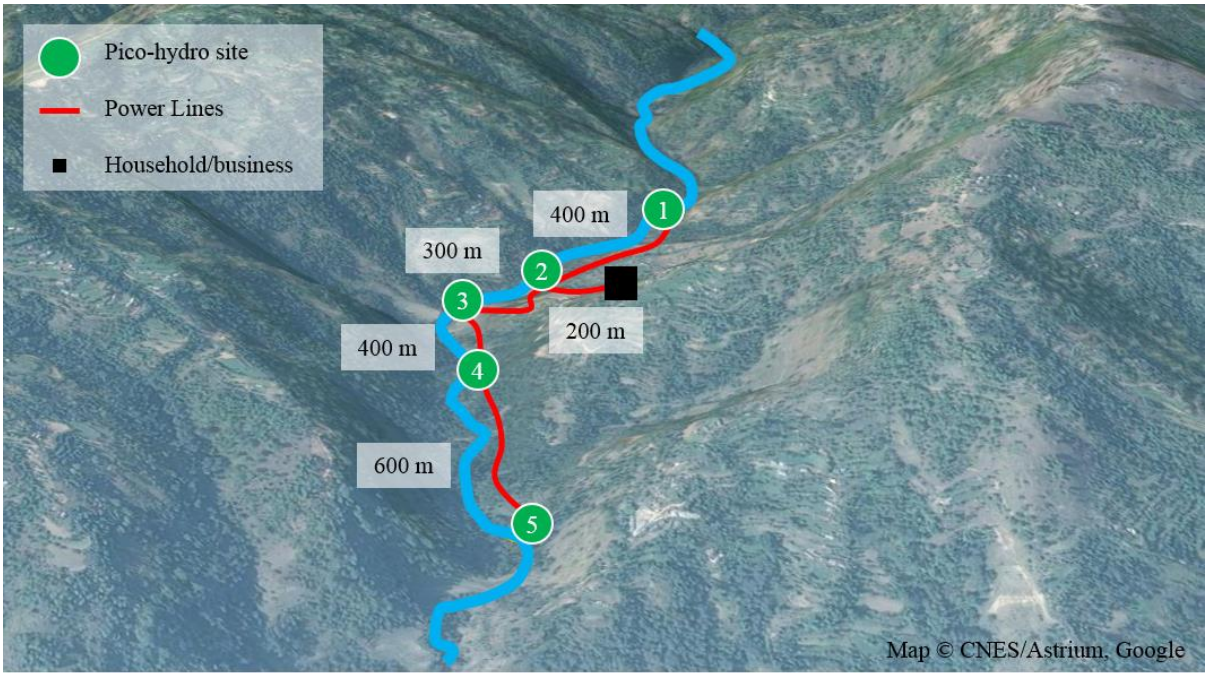

Figure 17: Potential pico-hydro off-grid network on the Patan Khola, Bhanbhane District, Western Nepal.

At site 3, there is 5 m of available head. As the low head Turgo turbine in [9] is only rated to 3.5 m head, an additional generator unit is added to make use of the remaining 1.5 m of head. The model and control that has been developed in the previous sections is then used to develop the grid. For this modelling of the implementation site therefore, 6 generator units

(GU) are connected to the network with ACSR transmission lines and two linear 1 kVA, 0.9 p.f. loads at the load centre. Initially, GU 2 – 6 are connected to the network, with a 1 kVA load. After 10 seconds, GU 1 is connected, and after 15 seconds the second 1 kVA load is also connected. After 20 seconds, the head at GU 2 reduces from 3.5 m to 1.5 m, representing an instantaneous change in environmental conditions, such as a blockage of the intake. The results from this simulation are shown in Fig. 18.

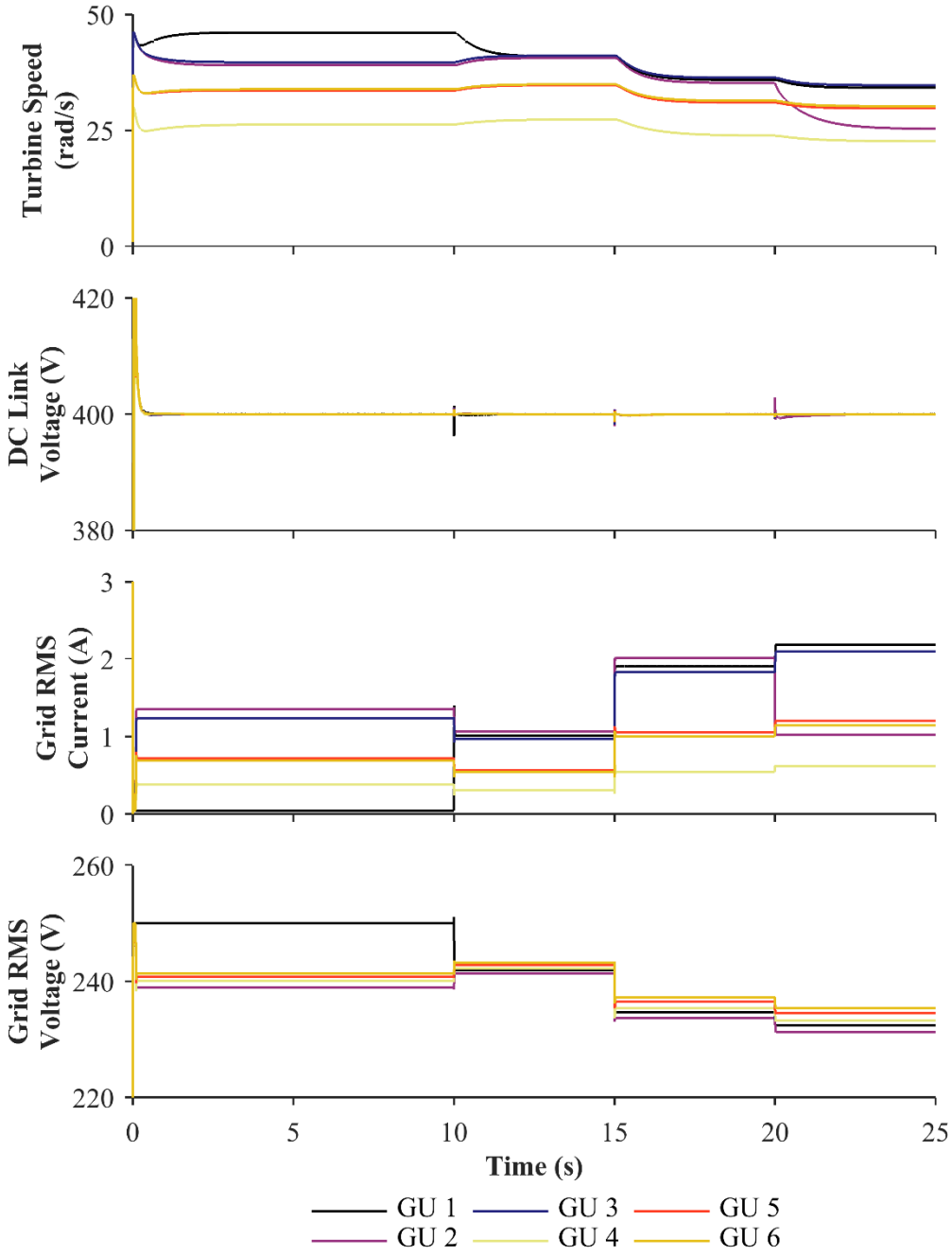

Figure 18: A 6 unit pico-hydro off-grid network operating with different heads. After 10 seconds one unit is connected to the network, and after 15 seconds an additional load is added.

As can be seen in Fig. 18, once the units have reached a steady state in current and speed, GU 1 is added. This causes the load on all the other generator units to drop, with the current decreasing, and therefore the turbine rotational speed increases. At this point, GU 2 is closest to the load and has the maximum head, therefore it supplies the most current to the

load. Conversely, GU 4 has the lowest current output as it has the lowest head. When the head at GU 2 drops from 3.5 to 1.5 m, the current output in all the other generator units increases, whilst that from GU 2 reduces from 2 A_{RMS} to 1 A_{RMS}.

1.7. Hybrid Renewable Off-Grid Network

An extension of the off-grid pico-hydropower grid is to hybridise it with other renewable technologies such as solar PV or small scale wind turbines, as shown in Fig. 19.

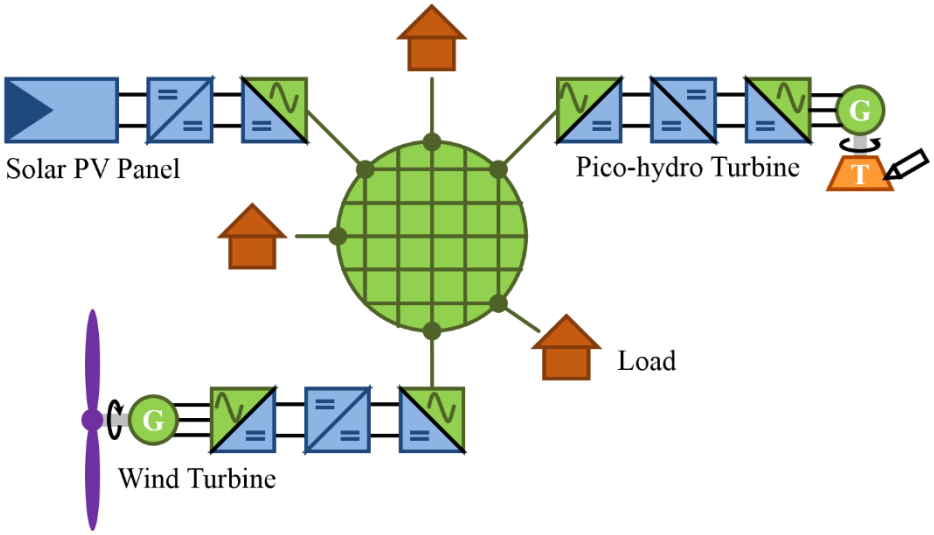

Figure 19: Hybrid renewable off-grid network with pico-hydropower, solar PV and wind turbine.

The same inverter interface can be used to control each of these sources, with minor changes to the rest of the hardware and control algorithm.

1.7.1. Solar PV Interface Modifications

The solar PV array outputs DC power, so the rectifier stage is not required in the power conversion. The array is assumed to have a 1 kWp output, with a maximum power point tracking algorithm. The power ratio that was previously used to modify the droop coefficients, γ, for the solar PV is calculated by

$$\gamma_{PV} = P_{PV,MPPT}/P_{PV,MAX} \qquad (22)$$

where γ_{PV} is the PV power ratio, $P_{PV,MPPT}$ is the measured maximum power from the PV array and $P_{PV,MAX}$ is the maximum rated power from the PV array.

1.7.2. Wind Turbine Interface Modifications

The wind turbine is assumed to feed directly into the rectifier, as with the pico-hydro turbine. An alternative would be to include some energy storage on the rectified DC stage, which would smooth the power generated from gusts, however this is not included for this simulation. The turbine is assumed to have a maximum electrical power output of 1 kW. As with the solar PV array, the power ratio to modify the droop coefficients becomes

$$\gamma_{WD} = P_{WD,MEAS}/P_{WD,MAX} \qquad (23)$$

where γ_{WD} is the wind turbine power ratio, $P_{WD,MEAS}$ is the measured maximum power from the wind turbine and $P_{WD,MAX}$ is the maximum rated electrical power from the turbine.

1.7.3. Hybrid Grid Simulation

The hybrid grid is assumed to be as drawn in Fig. 19, with a single pico-hydro turbine, wind turbine and solar PV array connected to it. Each source is assumed to be 1km radially from the load. The solar panels are assumed to be 5 parallel connected PV modules and modelled using a standard PV model [44]. The wind turbine is modelled as a locally manufactured Piggott Turbine [45] using the model in [46]. The pico-hydro turbine has a constant head of 3.5 m. The irradiance of the PV array starts at 500 W/m² and increases to 1000 W/m² after 10 seconds, simulating the panel moving out of shade. The wind turbine sees a Gaussian distribution of wind speed of with a mean of 10 m/s and variance of 3 m/s. A 500 VA 0.9 p.f. load is connected after 5 seconds, then after 15 seconds the load increases to 1500 VA.

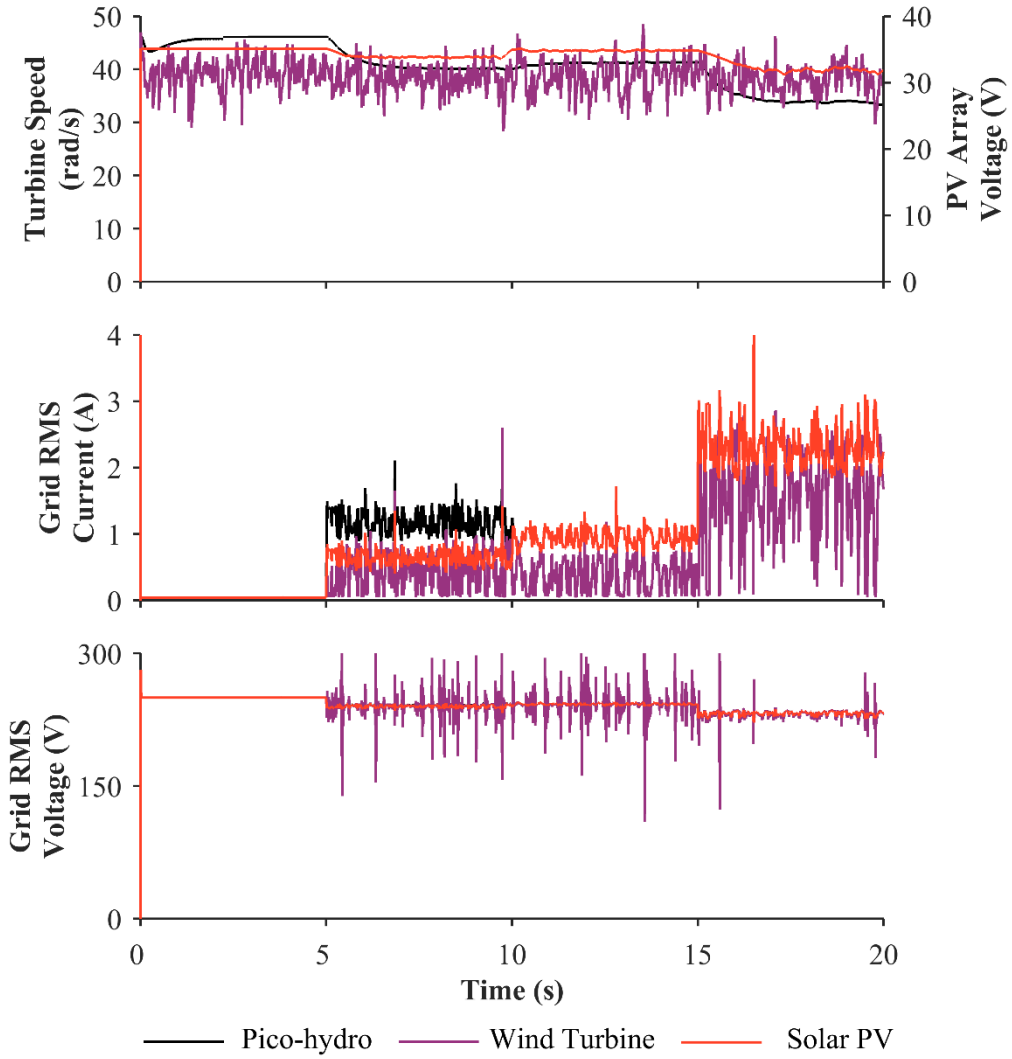

Figure 20: Turbine speed, PV voltage and output current and voltage from hybrid off-grid network.

As can be seen from Fig. 20, the inverter interfaces operate similarly to the pico-hydropower network, with each system feeding in dependent on its available power. Therefore, initially with the solar PV able to supply half its rated power, it supplies approximately half the current of the hydro turbine. As the wind turbine power is constantly varying, so does the current input into the network. The solar PV and hydro are able to support this varying

current. If increased energy storage was added to the wind turbine system, this could become more constant, and smoothing out the supply from the wind turbine.

1.8. Summary

This chapter has introduced the concept of the pico-hydropower off-grid network, shown the proposed control design for the power electronic interface and developed the models of the system to show the performance. The system is simulated initially with a single generator unit, demonstrating the voltage droop, and the performance of the system when connected to a non-linear load. Following this, two generator units are simulated, showing how the power sharing alters as the distance between the generators and load becomes unequal and how as the input power to the turbine, calculated from the head, the power sharing ratio also changes. This simulation is then expanded to cover an example implementation site with multiple turbines, showing similar results in a changing environment. Finally, the pico-hydropower off-grid network concept is extended to include additional renewable resources of solar PV and wind turbines, with minor control modifications, and a simulation demonstrates how this could operate with changing loads and changing input powers.

1.9. Further Reading

- Jenkins N., Ekanayake J. B., Strbac G., *Distributed Generation*, London: IET, 2010.
- Zhong Q. C. and Hornik T., *Control of Power Inverters in Renewable Energy and Smart Grid Integration*, Chichester: John Wiley & Sons Ltd, 2013.
- Harvey A., Brown A., Hettiarachi P., Inversin A., Micro Hydro Design Manual: A Guide to Small Scale Water Power Schemes, Rugby: Practical Action Publishing, 1993.
- Practical Action, *Poor People's Energy Outlook*, Rugby: Practical Action Publishing, 2010 - 2014.
- Williamson S. J, Griffo A., Stark B. H., Booker J. D., "A controller for single-phase parallel inverters in a variable-head pico-hydropower off-grid network," Sustainable Energy, Grids and Networks, vol. 5, pp. 114-124, 2016.

References

[1] International Energy Agency, "World Energy Outlook," Organization for Economic Co-operation and Development, London, 2014.

[2] Smith N. P. A., "Induction generators for stand-alone micro-hydro systems," Proceedings of International Conference on Power Electronics, Drives and Energy Systems for Industrial Growth, New Delhi, 1996, pp. 669-673.

[3] Maher P., *The Pico Power Pack: Fabrication and Assembly Instructions* [online], May 2001. Available from www.picohydro.org.uk.

[4] Taylor S. D., Fuentes M., Green J. and Rai K., *Stimulating the Market for Pico-hydro in Ecuador*, Department for International Development Report R8150, London, 2003.

[5] Williams A. A. and Simpson R., "Pico hydro - Reducing technical risks for rural electrification," Renewable Energy, vol. 34, pp. 1985-1991, 2009.

[6] Energy Sector Management Assistance Program, *Technical and Economic Assessment of Off-grid, Mini-grid and Grid Electrification Technologies*, World Bank Report, New York, 2007.

[7] Strauss P. and Angler A., "AC coupled PV hybrid systems and microgrids – state of the art and future trends," Proceedings of 3rd World Conference on Photovoltaic Energy Conversion, Osaka, 2129 – 2134, 2003.

[8] Guerrero J. M., Matas J., de Vicuna L. G., Castilla M. and Miret J., "Decentralized Control for Parallel Operation of Distributed Generation Inverters Using Resistive Output Impedance," IEEE Transactions on Industrial Electronics, vol. 54, no. 2, pp. 994-1004, 2007.

[9] Williamson S. J., Stark B. H. and Booker J. D., “Performance of a low-head pico-hydro Turgo turbine,” Applied Energy, vol. 102, pp. 1114-1126, 2013.
[10] Márqueza J. L., Molinab M. G., and Pacasc J. M., “Dynamic modeling, simulation and control design of an advanced micro-hydro power plant for distributed generation applications,” International Journal of Hydrogen Energy, vol. 35, pp. 5772–5777, 2010
[11] Muller G. and Senior J., “Simplified theory of Archimedean screws,” Journal of Hydraulic Research, vol. 47, pp. 666–669, 2009.
[12] Williamson S. J., Stark B. H. and Booker J. D., “Low head pico hydro turbine selection using a multi-criteria analysis,” Renewable Energy, vol. 61, pp 43-50, 2014.
[13] Williamson S. J., Stark B. H. and Booker J. D., “Modelling of a Multi-Source Low-Head Pico Hydropower Off-Grid Network,” Proceedings of IEEE International Conference on Sustainable Energy Technologies, Kathmandu, 2012, pp. 369-374.
[14] Herold T., Franck D., Lange E. and Hameyer K., “Extension of a D-Q Model of a Permanent Magnet Excited Synchronous Machine by Including Saturation, Cross-Coupling and Slotting Effects,” Proceedings of IEEE International Electric Machines & Drives Conference, Niagara Falls, 2011, pp. 1363-1367.
[15] DVE generator PMGO–1,5K–200 (http://www.dvetech.dk).
[16] Mohan N.,. Undeland T. M and Robbins W. P., *Power Electronics: Converters, Applications, and Design*, New York: John Wiley & Sons, 2003.
[17] Erikson R. W. and Maksimovic D., *Fundamentals of Power Electronics*, New York: Springer-Verlag, 1998.
[18] Notton G., Lazarov V., Stoyanov L. and Heraud N., “Grid–Connected Photovoltaic System: Optimization of the Inverter Size Using an Energy Approach,” Proceedings of International Symposium on Advanced Electromechanical Motion Systems & Electric Drives, Lille, 2009.
[19] ESMAP/UNDP, *Mini Grid Design Manual*, ESMAP, Washington DC, 2000.
[20] Liang X. and Ilochonwu O., “Induction Motor Starting in Practical Industrial Applications,” IEEE Transactions on Industry Applications, vol. 47, no. 1, pp. 271-280, 2011.
[21] Monfared M., Golestan S., Guerrero J. M., “Analysis, Design, and Experimental Verification of A Synchronous Reference Frame Voltage Control for Single-Phase Inverters,” IEEE Transactions on Industrial Electronics, vol. 61, pp. 258-269, 2014.
[22] Zhong Q. C. and Zeng Y., “Parallel Operation of Inverters with Different Types of Output Impedance”, Proceedings of IEEE Industrial Electronics Conference, Vienna, 2013, pp. 1398-1403.
[23] Zhong Q. C., “Robust droop controller for accurate proportional load sharing among inverters operated in parallel,” IEEE Transactions on Industrial Electronics, vol. 60, pp. 1281-1290, 2013.
[24] de Brabandere K., Bolsens B., Van den Keybus J., Woyte A., Driesen J., Belmans R., “A Voltage and Frequency Droop Control Method for Parallel Inverters,” IEEE Transactions on Power Electronics, vol. 22, pp. 1107-1115, 2007.
[25] E. Clarke, *Circuit Analysis of AC Power Systems*, New York: Wiley, 1943, vol. I.
[26] Roshan A., Burgos R., Baisden A.C., Wang F., Boroyevich D., “A D-Q Frame Controller for a Full-Bridge Single Phase Inverter Used in Small Distributed Power Generation Systems,” Proceedings of IEEE Applied Power Electronics Conference, Anaheim, 2007, pp. 641-647.
[27] Burger B. and Engler A., “Fast Signal Conditioning in Single Phase Systems,” Proceedings of European Power Electronics and Drives Conference, Graz, 2001.
[28] Ciobotaru M., Teodorescu R., and Blaabjerg F., “A New Single-Phase PLL Structure Based on Second Order Generalised Integrator,” Proceedings of IEEE Power Electronics Specialists Conference, Jeju, 2006, pp. 1-6.
[29] de Brabandere K., Loix T., Engelen K., Bolsens B., Van den Keybus J., Driesen J., Belmans R., “Design and Operation of a Phase-Locked Loop with Kalman

Estimator-Based Filter for Single-Phase Applications," Proceedings of IEEE Conference on Industrial Electronics, Paris, 2006, pp. 525-530.
[30] Lascu C., Asiminoaei L., Boldea I., and Blaabjerg F., "Frequency response analysis of current controllers for selective harmonic compensation in active power filters", IEEE Transactions on Industrial Electronics, vol. 56, pp.337 -347, 2009.
[31] Zhang R., Cardinal M., Szczesny P., and Dame M., "A grid simulator with control of single-phase power converters in D-Q rotating frame," in Proceedings of IEEE Annual Power Electronics Specialists Conference, Cairns, 2002, pp. 1431-1436.
[32] Micallef A., Apap M., Spiteri-Staines C., Guerrero J. M., and Vasquez J. C., "Reactive power sharing and voltage harmonic distortion compensation of droop controlled single phase islanded microgrids", IEEE Transactions on Smart Grid, vol. 5, pp. 1149-1158, 2014.
[33] Karimi-Ghartemani M., "Universal Integrated Synchronization and Control for Single Phase DC/AC Converters", IEEE Transactions on Power Electronics, vol. 30, pp. 1544 – 1557, 2015.
[34] Bahrani B., Saeedifard M., Karimi A., and Rufer A., "A Multivariable Design Methodology for Voltage Control of a Single-DG-Unit Microgrid", IEEE Transactions on Industrial Informatics, vol. 9, pp. 589-599, 2013.
[35] Bahrani B., Rufer A., Kenzelmann S., and Lopes L., "Vector control of single-phase voltage source converters based on fictive axis emulation", IEEE Transactions on Industrial Applications, vol. 47, pp.831-840, 2011.
[36] Marwali M. N., Jung J., and Keyhani A., "Control of Distributed Generation Systems – Part II: Load Sharing Control", IEEE Transactions on Power Electronics, vol. 19, pp. 1551-1531, 2004.
[37] Mattavelli P., "A closed-loop selective harmonic compensation for active filters", IEEE Transactions on Industrial Applications, vol. 37, pp. 81-89, 2001.
[38] Xiaoming Y., Merk W., Stemmler H., Allmeling J., "Stationary-frame generalized integrators for current control of active power filters with zero steady-state error for current harmonics of concern under unbalanced and distorted operating conditions", IEEE Transactions on Industrial Applications, vol.38, pp. 523-532, 2002.
[39] Golestan S., Monfared M., Freijedo F. D., Guerrero J. M., "Dynamics Assessment of Advanced Single-Phase PLL Structures," IEEE Transactions on Industrial Electronics, vol. 60, pp. 2167-2177, 2013.
[40] Golestan S., Monfared M., Freijedo F. D., and Guerrero J. M., "Advantages and Challenges of a Type-3 PLL," IEEE Transactions on Power Electronics, vol. 28, pp. 4985-4997, 2013.
[41] Geng H., Sun J., Xiao S., Yang G., "Modeling and Implementation of an All Digital Phase-Locked-Loop for Grid-Voltage Phase Detection", IEEE Transactions on Industrial Informatics, vol. 9 pp. 772-780, 2013.
[42] Rodriguez P., Luna A., Candela I., Mujal R., Teodorescu R., and Blaabjerg F. "Multiresonant frequency-locked loop for grid synchronization of power converters under distorted grid conditions", IEEE Transactions on Industrial Electronics, vol. 58, pp. 127-138, 2011.
[43] Guerrero J. M., Vasquez J. C., Matas J., de Vicuna L. G., Castilla M., "Hierarchical Control of Droop-Controlled AC and DC Microgrids—A General Approach Toward Standardization", IEEE Transactions on Industrial Electronics, vol. 58, pp. 158-172, 2011.
[44] Villalva M. G., Gazoli J. R., and Filho E. R., "Comprehensive Approach to Modeling and Simulation of Photovoltaic Arrays," IEEE Trans. Power Electron., vol. 24, pp. 1198-1208, 2009.
[45] Monteiro J. P., Silvestre M. R., Piggott H., Andre J. C., "Wind tunnel testing of a horizontal axis wind turbine rotor and comparison with simulations from two Blade Element Momentum codes," Journal of Wind Engineering and Industrial Aerodynamics, vol. 123 part A, pp 99-106, 2013.

[46] Bolte E., Landwehr M., “Mathematical model of small wind turbines,” in Proceedings of 9th International Conference on Ecological Vehicales and Renewable Energies, pp 1-6, 2014.